Nanoscale

ROYAL SOCIETY OF CHEMISTRY

PAPER

View Article Online
View Journal | View Issue

Cite this: *Nanoscale*, 2023, **15**, 3300

Spin-photogalvanic effect in chiral lead halide perovskites

Ruiheng Pan,[a] Xiantong Tang,[a] Lixuan Kan,[b,c] Yang Li,[b,c] Haomiao Yu [b,c] and Kai Wang *[b,c]

Received 10th December 2022,
Accepted 16th January 2023

DOI: 10.1039/d2nr06919a

rsc.li/nanoscale

Low-temperature solution-made chiral lead halide perovskites (LHPs) have spontaneous Bychkov–Rashba spin orbit coupling (SOC) and chiral-induced spin selectivity (CISS) qualities. Their coexistence may give rise to considerable spin and charge conversion capabilities for spin-orbitronic applications. In this study, we demonstrate the spin-photogalvanic effect for $(R\text{-MBA})_2PbI_4$ and $(S\text{-MBA})_2PbI_4$ polycrystalline film-based lateral devices (100 μm channel length). The light helicity dependence of the short-circuit photocurrent exhibits the circular photogalvanic effect (CPGE) and linear photogalvanic effect (LPGE) with decent two-fold symmetry for a complete cycle in a wide temperature range from 4 K to 300 K. Because of the Rashba SOC and the material helicity, the effect is converse for the two chiral LHPs. In addition, its magnitude and sign can be effectively tuned by constant magnetic fields. The Rashba effect, CISS-generated unbalanced spin transport, and chiral-induced magnetization are mutually responsible for it. Our study evidently proves the future prospect of using chiral LHPs for spin-orbitronics.

1. Introduction

Low-temperature solution processable lead halide perovskites (LHPs) have received unprecedented attention because of their potential applications in highly efficient solar cells and light emitting diodes (LEDs).[1–9] In addition to desirable optoelectronic properties such as high mobilities, strong photo-absorption strengths and high color purities for light emissions, LHPs are known to exhibit strong spin–orbit coupling (SOC) due to the existence of heavy chemical constituents such as lead (Pb) and iodine(I).[10–13] This results in degenerated energy band splitting in the momentum vector space. In addition, most of them possess the crystalline structure inversion asymmetry (SIA). As a result, the so-called Bychkov–Rashba SOC can be made possible.[14,15] All of these factors ensure that LHPs are promising to the development of spin-orbitronics,[16] in which electronic spins act as information carriers and quantum bits for data transmission and storage. This has led to the studies of magnetic spin-valves,[17] magneto-optics,[18,19] and spin-LEDs.[20] Recently, some experiments and theories have pointed out that their spin-optoelectronic properties can be extensively modified by introducing chiral organic ligands into the inorganic crystalline frameworks. This yields Ruddlesden–Popper (RP) two-dimensional (2D) chiral LHPs.[21–23] The implementation of the chiral organic ligands may also bring in switchable ferroelectric property, which offers an additional degree of freedom for the manipulation of Rashba bands through externally applied electrical fields.[24,25] To date, they have been studied for applications in circularly polarized luminescence (CPL),[26] nonlinear optics,[27] magneto-optics,[28] spin-transport[29] and spin-LEDs.[30–32] CPL cannot be easily achieved in achiral LHPs unless ultrahigh magnetic fields are involved.[33]

With this regard, we have successively synthesized the chiral LHPs based on $(R\text{-MBA})_2PbI_4$ and $(S\text{-MBA})_2PbI_4$ (MBA = $C_6H_5C_2H_4NH_3$), while demonstrating the magnetic field manipulation of CPL and magneto-photoluminescence (magneto-PL) from both experimental and theoretical aspects in 2021.[28] We found that the connection among the exciton's wavevector (K), material helicity (τ) and effective spin–orbit coupling strength (α) are mutually responsible for the exciton's dispersion relation.[34,35] Despite the photo-induced CPL, we think it is of equal importance to study the photo-induced electrical transport in term of the short-circuit photocurrent for the chiral LHP system. Because of the naturally crystalline property, SIA and chiral-induced spin selectivity (CISS) are expected to contribute for the spin-photogalvanic effect.[36–38]

[a]*School of Science, Chongqing University of Posts and Telecommunications, Chongqing, 400065, China*
[b]*Key Laboratory of Luminescence and Optical Information, Ministry of Education, School of Physical Science and Engineering, Beijing Jiaotong University, Beijing, 100044, China. E-mail: kaiwang@bjtu.edu.cn*
[c]*Institute of Optoelectronics Technology, Beijing Jiaotong University, Beijing, 100044, China*

Moreover, the temperature and field dependences remain unknown for the chiral LHP system.

In the system, the light helicity (*i.e.*, circular and linear polarization) dependent photocurrent with the absence of a bias voltage can produce the circularly photogalvanic effect (CPGE) and linear photogalvanic effect (LPGE). The magnitude of the photocurrent varies periodically with respect to the changing polarization. The CPGE can be thought of as a transfer from the light angular moment to a directional free charge carrier. The effect is recognized as one of the crucial methods to validate the Rashba band splitting.[12,39,40] It appears in polar semiconductors,[41] topological insulators,[42,43] and 2D electron gas-based semiconductor quantum well structures.[36,44] Recently, the CPGE was also demonstrated in 2D layered hybrid perovskite single crystals and chiral 2D organic–inorganic hybrid perovskites.[39,45] Two prerequisites are required to realize it. One is the photoelectrical response capability, while another criterion is an unbalanced spin-dependent electronic transport due to the presence of degenerated Rashba bands. The former one can be satisfied by choosing an appropriate photoexcitation source. Moreover, the latter one can be made possible by the chiral LHPs since they possess inherently crystalline inversion symmetry breaking. Additionally, the chiral-induced spin selectivity (CISS) may facilitate the spin-dependent electronic transport because of the inherent chiral-induced SOC.

In this work, we synthesized and fabricated lateral spin-orbitronic devices. For concreteness, we chose $(R\text{-MBA})_2PbI_4$ and $(S\text{-MBA})_2PbI_4$ as the chiral LHPs. Both can form high quality polycrystalline films with certain growth modes on soda-lime glass substrates. A pronounced spin-photogalvanic effect can be detected in a wide temperature range from 4 K to 300 K. The effect is attributed to the interplay of the perovskite Rashba band and CISS.

2. Experiments

2.1 Materials and device fabrication

In our experiments, all chemicals were commercially available products and could be used without further purifications. Both prototypical chiral perovskites, for instance (*R*)-(+)-α-methylbenzylamine (*R*-MBA, 98%, optical purity >97%) and (*S*)-(−)-α-methylbenzylamine (*S*-MBA, 98%, optical purity >97%), were chosen. More details about the single crystal syntheses can be read from our early papers.[35] In short, 200 mg of lead oxide (PbO), 200 μl *R*- or *S*-MBA, and 6 ml of aqueous hydriodic acid (HI) were mixed in a glass vial. The mixture naturally led to some yellow precipitates. Then, it was placed in an oil bath. The solution experienced a thermal treatment at 100 °C in order to dissolve the precipitates. After this, it was naturally cooled down to room temperature. We observed many orange needle-like monocrystals. They were filtrated and rinsed with toluene several times. Finally, they were all dried in an oven for several hours.

Prior to the device fabrication, transparent glass substrates were cleaned by a standard chemical method using acetone, isopropanol and ethanol in an ultrasonic bath. After drying, they were treated by plasma oxidation for approximately 1 min. The precursor solutions of chiral LHPs were prepared by dissolving the pre-prepared single crystals (20 wt%) in *N*,*N*-anhydrous dimethylformamide (DMF) organic solvent. Thin films were fabricated by the conventional spin-coating method on top of the substrates with a spinning speed and time of 4000 rpm and 30 s, respectively. All of the samples were subsequently annealed at 100 °C for 8 min. After this, they were transferred into an integrated thermal evaporation system. Then, 80 nm thick gold (Au) electrodes were deposited onto the top surfaces of the films. The channel length for charge transport was approximately 100 μm.

2.2 Material characterization and transport measurements

The morphologies of the chiral HOIPs thin films were examined by a field emission scanning electron microscope (SEM, JSM-6700F) system. Ultraviolet–visible photo-absorption spectra were conducted by a spectrometer (UV-2600). The measurement of the transmission circular dichroism (CD) was performed by a Jasco CD spectrometer (J-1500). The crystalline phases of $(R\text{-MBA})_2PbI_4$ and $(S\text{-MBA})_2PbI_4$ pristine films were analyzed by an X-ray diffraction (XRD) system (Bruker D-8 Advance). During the transport measurements, the devices were mounted onto a self-designed sample holder. This holder was placed inside a cryogenic closed-cycle system. The complete system was located in-between a pair of electromagnets. A semiconductor laser diode (405 nm), combined with a set of linear and circular polarizers were used as the photoexcitation source. The device could be illuminated by the laser beam through a viewing port, and electrical signals could be recorded *via* a source-meter unit.

3. Results and discussion

We began with the fundamental characterization of the material property. The polycrystalline film surface morphologies and roughness of $(R\text{-MBA})_2PbI_4$ and $(S\text{-MBA})_2PbI_4$ were characterized by SEM, as shown in Fig. 1(a) and (b), respectively. They have similar morphologies. In order to validate the successful implementation of chirality into the LHPs, the CD property was examined and the spectra are given in Fig. 1(c) for $(R\text{-MBA})_2PbI_4$ and $(S\text{-MBA})_2PbI_4$. The CD spectra manifest the mirror symmetry with the common photo-absorption band-edge at about 518 nm (*i.e.*, 2.39 eV). In Fig. 1(d), the UV-visible photo-absorption peaks that occur at 334 nm and 370 nm are ascribed to bound exciton transitions.[46] Such absorption band-edge is consistent with the CD spectra. Fig. 1(e) shows the CPL spectra for the $(R\text{-MBA})_2PbI_4$ and $(S\text{-MBA})_2PbI_4$ polycrystalline films with the dominant emissive peaks at approximately 515 nm. The spectra are symmetric with respect to each other, indicating their chiral character. The crystallinities of the films are revealed by the out-of-plane

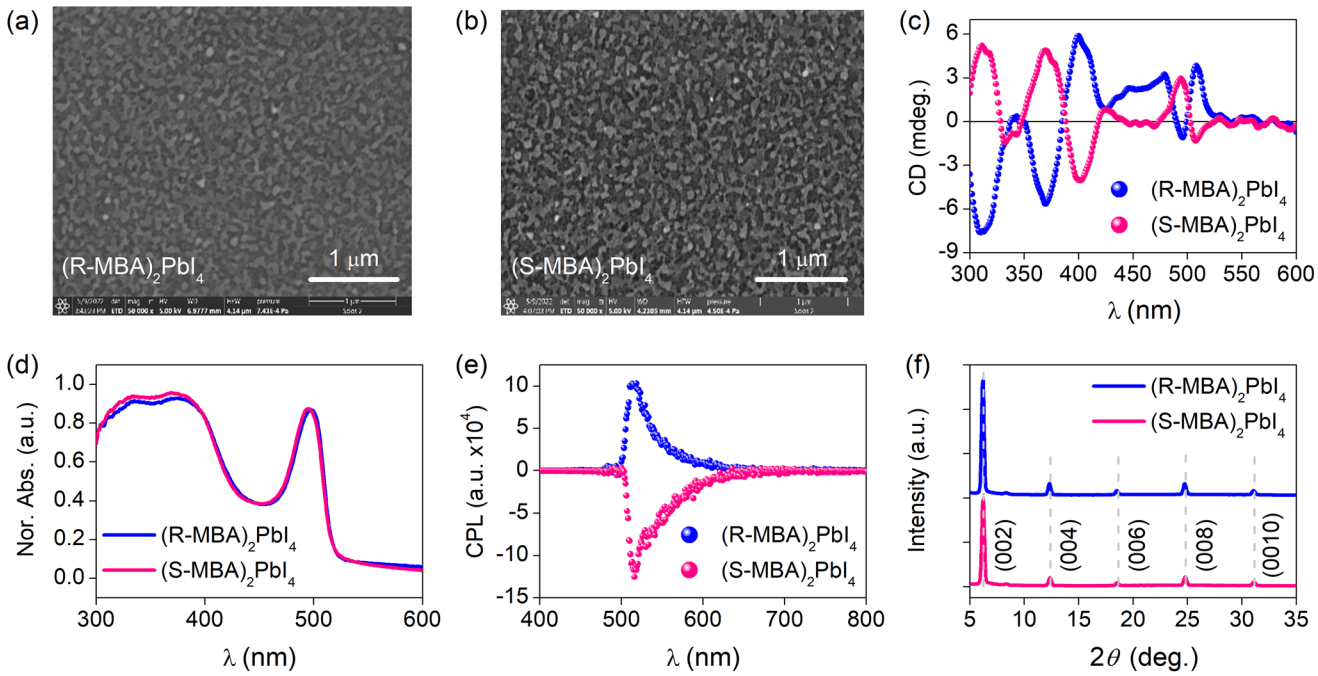

Fig. 1 (a) and (b) are SEM surface morphologies for $(R\text{-MBA})_2PbI_4$ and $(S\text{-MBA})_2PbI_4$ polycrystalline films, respectively. (c)–(f) are their CD spectra, UV-visible absorption spectra, CPL spectra and XRD spectra, respectively.

XRD spectra in Fig. 1(e). By indexing, the spectra contain successively diffracted bands at 2θ = 6.18°, 12.32°, 18.50°, 24.74°, and 31.06°, which correspond to the (002), (004), (006), (008) and (0010) crystalline phases, respectively.[46,47]

Fig. 2(a) shows the lateral device structure on top of the glass substrate. It consists of Au/$(R\text{-MBA})_2PbI_4$ (or, $(S\text{-MBA})_2PbI_4$)/Au. Judging from the inset SEM image, the channel length was designed and fabricated to be approximately 100 μm. Such channel length guarantees that the photogenerated spin-transport takes place within its coherent length. Owing to the existence of the material chirality, we expected to observe remarkable responses of polarized light-induced photoluminescence. Fig. 2(b) and (c) show the experimental results of the light polarization-dependent PL intensities for $(R\text{-MBA})_2PbI_4$ and $(S\text{-MBA})_2PbI_4$, respectively. During the measurements, a quarter-wave plate (QWP) could be rotated in-plane. The PL intensity varies according to PL (σ^+) > PL (linear) > PL (σ^-) for $(R\text{-MBA})_2PbI_4$ (Fig. 2(a)). It is *vice versa* for $(S\text{-MBA})_2PbI_4$ due to their chirality (Fig. 2(c)). It should be noted that the linearly polarized photoexcitation acts as the superposition for an equal amount of the left- and right-handed circularly polarized photoexcitation.

With the same devices, we carried on with the CPGE measurement. In this case, QWP was used to generate the polarization state for the incident light. The rotational angle (α) was defined by the angular rotation of QWP with respect to

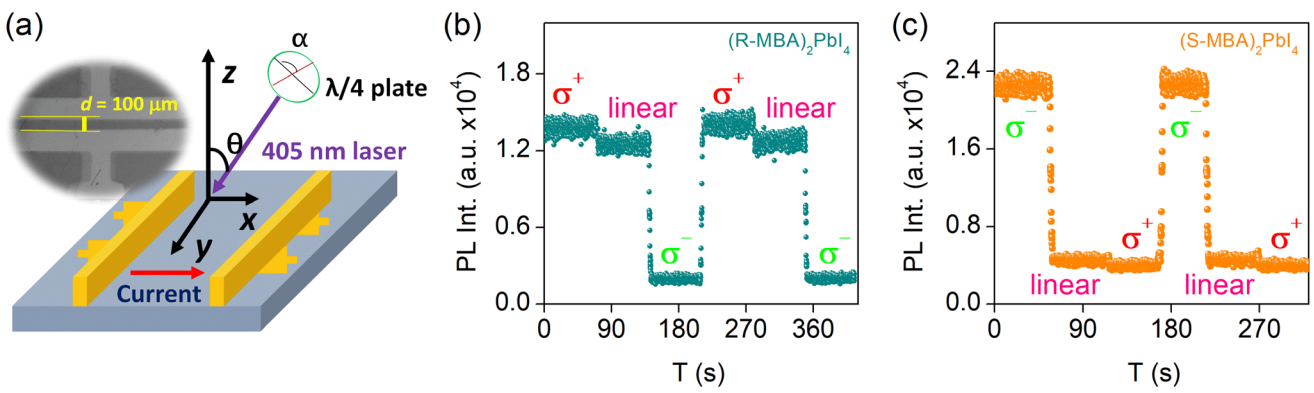

Fig. 2 (a) The schematic drawing of the lateral device configuration Au/chiral LHP/Au. The inset image shows the channel length of approximately 100 μm. (b) and (c) are the variations of the PL intensities due to the alternative switches among the left-, linear and right-circularly polarized photoexcitation for $(R\text{-MBA})_2PbI_4$ and $(S\text{-MBA})_2PbI_4$, respectively. The photoexcitation wavelength and the laser power were 405 nm and 90 mW, respectively.

its fast axis. The photocurrent was continuously recorded at different angles. Fig. 3(a) and (b) are the experimental results of the in-plane photocurrent as a function of α for $(R\text{-MBA})_2PbI_4$ and $(S\text{-MBA})_2PbI_4$ at 4 K, respectively. The purple solid lines are the corresponding fitting curves. The schematic illustrations for the light helicity are listed on top of the figures. In both devices, the variations of the photocurrent through the complete cycle are mainly determined by the helicity of the incident light. The switches among the left- (σ^+), linear ($\sigma^+ + \sigma^-$), and right- (σ^-) circularly polarized light lead to the periodic change of the photocurrent within the full revolution. Notably, the photocurrent generation due to the linearly polarized light is indeed the linear photogalvanic effect (LPGE). We confirmed that the magnitude of CPGE mainly relies on the helicity of the chiral LHPs since their left and right handedness are reflected from the signals. Fig. 3(c) provides the temperature dependence of the effect from 4 K to 300 K for $(R\text{-MBA})_2PbI_4$. It remains considerably large at 300 K, and the effect is greatest at 4 K. The increase of the temperature smears out the spin-related effect due to the thermal disturbance of photoexcited polarized electrons. Such temperature dependence can be equally measured for $(S\text{-MBA})_2PbI_4$. Even for a crystalline inversion asymmetric material, the Rashba effect may be overruled at higher temperatures. The complete lineshape of the spin-photogalvanic effect can be well fitted by the analytical expression:

$$I_{xy}(\alpha) = C\sin(2\alpha) + L\cos(4\alpha) + D, \quad (1)$$

where sin (2α) and cos (4α) represent the lineshapes of CPGE and LPGE, respectively. The coefficients C and L denote the photocurrent for CPGE and LPGE, respectively. D is a polarization-independent quality that stems from some factors, including photothermal response and photo-Dember effect.[37,48,49] As we can see from the inset plot of Fig. 3(c), the C-value that reflects CPGE tends to decrease with the increase of temperature. More intriguingly, we observed that the applied magnetic

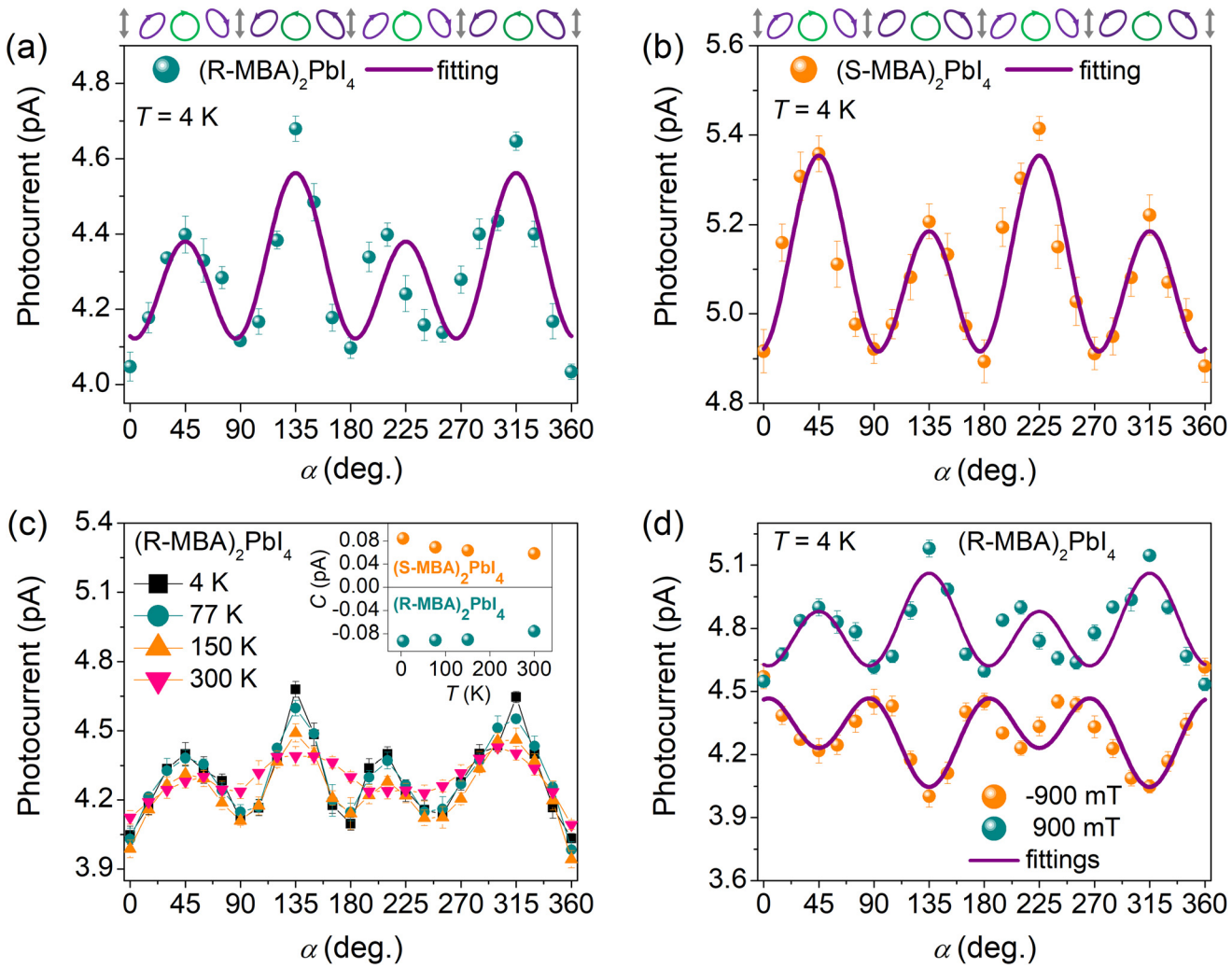

Fig. 3 Experimental results of spin-photogalvanic effect for (a) $(R\text{-MBA})_2PbI_4$ and (b) $(S\text{-MBA})_2PbI_4$. (c) and (d) are the temperature and magnetic-field dependent spin-photogalvanic effect for $(R\text{-MBA})_2PbI_4$. The inset of (c) shows the C value at different temperatures for $(R\text{-MBA})_2PbI_4$ and $(S\text{-MBA})_2PbI_4$, respectively. The photoexcitation wavelength and the laser power were 405 nm and 90 mW, respectively.

field can tune the magnitude and sign for the spin-photogalvanic effect. As shown in Fig. 3(d) for the field-dependent spin-photogalvanic effect for $(R\text{-MBA})_2PbI_4$, a constant in-plane large magnetic field (such as +900 mT) can enhance its magnitude. On the other hand, the negative field (such as −900 mT) helps reverse the effect. In fact, with an external stimulus such as light, the photogenerated electrons experience a chiral-induced SOC, leading to a chiral-induced magnetization for the nonmagnetic chiral LHPs. Such magnetization can be further coupled with an adjacent ferromagnet, while both of them can be manipulated by an external field. Previously, the conducting atomic force microscopic technique-based electronic transport measurements demonstrated the hysteresis-shaped magnetoresistance with a single ferromagnet for the chiral LHPs.[47] In addition, the chiral-induced magnetization was found in optical Kerr measurements.[50] They experimentally proved that the different resistive states (high and low resistive states) and different magnitudes of Kerr angles could be realized when magnetic fields were applied through the opposite directions. In our experiment, we found that the spin-photogalvanic effect can be effectively tuned by the constant magnetic fields with the same magnitudes, but opposite signs.

In principle, the spin-photogalvanic effect in the chiral LHPs can be understood by considering their unique electronic structure and the CISS property. We think that both Rashba band-associated exciton states and CISS for the unbalanced charge transport are mutually responsible for the effect. The energy–momentum dispersion of the system is mainly decided by the Pb–I octahedral inorganic crystalline framework. The heavy chemical constituents (*i.e.*, Pb and I) and the breaking of the crystalline inversion symmetry give rise to the parabolic-like degenerate band splitting and nondegenerate Rashba effect (Fig. 4(a)).[14,51–54] With previously theoretical calculations using the effective mass model, the conduction bands (CB) of LHPs are constructed by Pb-6p and I-5s orbitals.[11,54] The basis functions for electronic spin states in CB can be written by,[11]

$$c_{+(-)} = -\frac{1}{\sqrt{2}}[X + (-)iY]\cos\xi\downarrow(\uparrow) - (+)Z\sin\xi\uparrow(\downarrow), \quad (2)$$

where the subscript +(−) denotes the up(down) component of the pseudo spin component. *X*, *Y*, and *Z* represent the Pb-6p_x, -6p_y and -6p_z atomic orbitals, respectively. The parameter ξ is determined by the physical quantities, such as atomic SOC strength (λ) and the crystal-field strength (δ) since $2\xi = 2\sqrt{2\lambda}/(\lambda - 3\delta)$. The basis functions of the electronic spin states in the valence bands (VB) are expressed as,

$$v_{+(-)} = S\uparrow(\downarrow), \quad (3)$$

A photogenerated exciton may be one of the four possible spin configurations; for instance, $c_+\bar{v}_+$, $c_-\bar{v}_-$, $c_+\bar{v}_-$ and $c_-\bar{v}_+$. The exciton states can be expressed by:

$$|\Gamma_1 = \frac{1}{\sqrt{2}}(|c_+\bar{v}_- - |c_-\bar{v}_+), \quad |\Gamma_2 = \frac{1}{\sqrt{2}}(|c_+\bar{v}_- + |c_-\bar{v}_+), \quad |\Gamma_5{}^{\pm} = |c_\pm\bar{v}_\pm \quad (4)$$

Γ_1, Γ_2, and $\Gamma_5{}^+$ represent the dark, polarization emission along the *z*-axis, and doubly degenerated circular polarizations, respectively (Fig. 4(b)).[28] A minute description of the exciton fine structure for LHPs has been previously reported in our early work.[35,46] Without magnetic fields, the Rashba field leads to energy degeneracy and the energy level exchange between Γ_1 and Γ_2. With applied fields, the fine structures of $\Gamma_5{}^+$ can be further tuned based on the Zeeman effect. The relative positions of the energy states $\Gamma_5{}^+$ and $\Gamma_5{}^-$ are decided by the chirality. The optical transition-associated exciton generation, recombination and dissociation can be well depicted by Fig. 4(a) and (c) for the chiral LHPs.

As we can see from Fig. 4(a) for the pictorial illustration of the Rashba bands, the CB minimum and the VB maximum contain the total angular momenta of J_h = 1/2 and J_e = 1/2, respectively.[11,54,55] The optical transitions obey the selection rule, and the change of the projected angular momentum is $\Delta m_J = \pm 1$ (Fig. 4(c)). When the incident light is continuously changed among the left, linear and right polarization, the photoexcited electron densities and occupations of electronic density of states (DOS) in the energy–momentum vector space are actually anisotropic. Because of the Rashba splitting, the spin-related carrier transports are in the opposite directions (*i.e.*, group velocity $v = \frac{1}{\hbar}\frac{dE}{dk}$) for $\pm k$. As a result, the photocurrents are unbalanced along the two directions. Because of the chirality, $(R\text{-MBA})_2PbI_4$ and $(S\text{-MBA})_2PbI_4$ respond distinctly to the circularly polarized light. The spin-photogalvanic effects for the two are inversely related.

The different number of photogenerated paramagnetic species can be further verified by the polarized light-induced EPR spectroscopy. Fig. 4(e) and (f) provide experimental results of the temperature-dependent EPR spectra for the $(R\text{-MBA})_2PbI_4$ single crystals under circularly polarized photoexcitation at 300 K and 150 K, respectively. The same thing can be applied for $(S\text{-MBA})_2PbI_4$.[35] The resonant peaks that appear at approximately 509 mT and 125 mT are attributed to the Pb^{3+} and Pb^+ species, respectively.[56] From the observation of the spectra, the decrease of the thermal energy leads to the increase of the spectral intensity, which is primarily due to the reduction of the spin dephase. More importantly, σ^+ generates much greater spectral intensities than those from σ^-. The results clearly indicate that the polarized light-induced paramagnetic species follow the material chirality. In addition, from the observation of the GIWAX spectrum of $(S\text{-MBA})_2PbI_4$ in Fig. 4(g), it is known that the film growth mode is the face-on configuration (Fig. 4(d)) along the *z*-direction. The result is consistent with the out-of-plane XRD spectra in Fig. 1(f). Consequently, the crystalline *c*-axis is expected to be outward in the direction perpendicular to the propagation direction of the polarized light (*z*-axis). As a matter of fact, the excitation transition is determined by the electric field vector (E_{xy}) with respect to the *c*-axis (Fig. 4(d)). When they are perpendicular, the optical transitions due to the $\Gamma_5{}^{\pm}$ symmetry can be effectively triggered. On the other hand, the Γ_2 symmetry is allowed when both are in parallel.

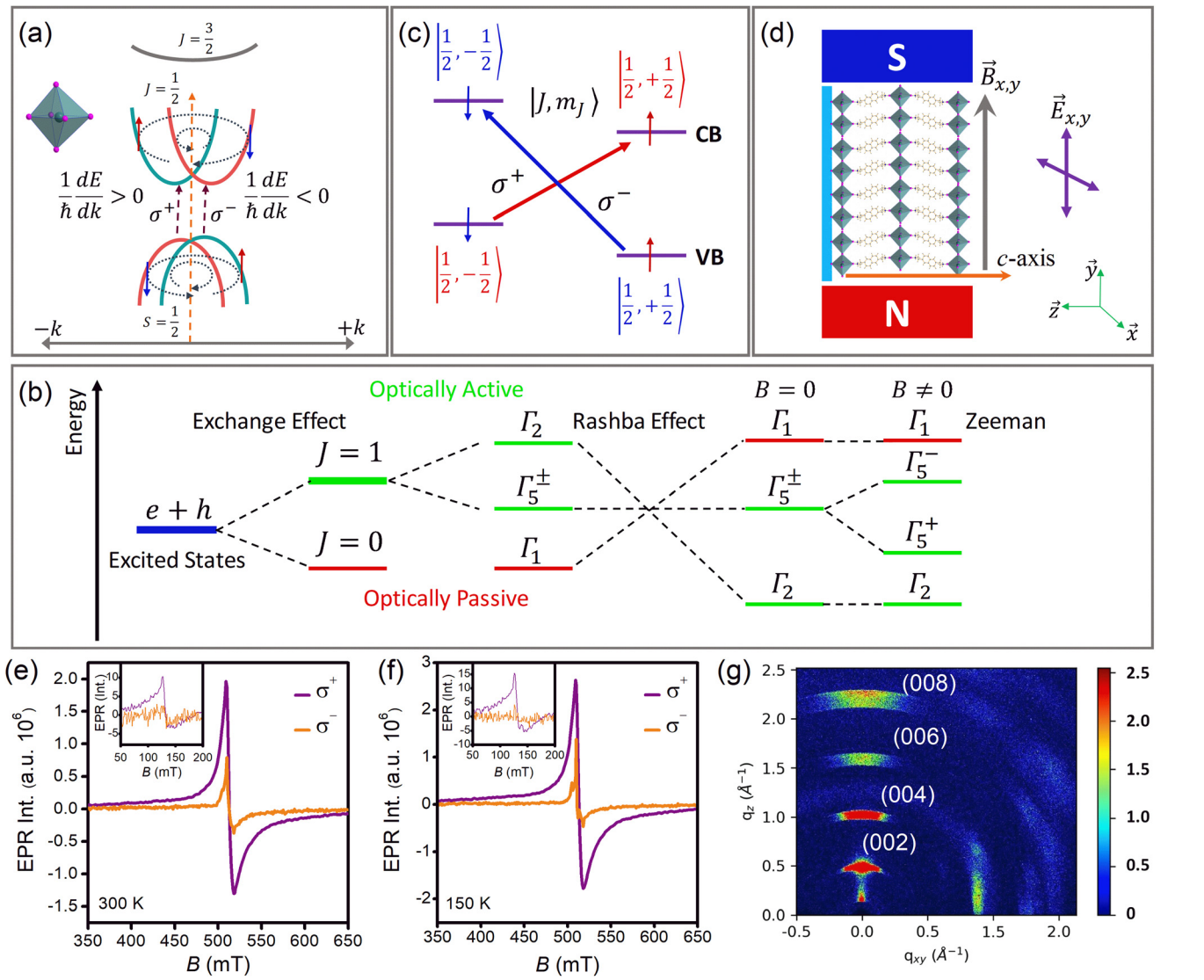

Fig. 4 (a) The pictorial illustration for the LHP Rashba band. (b) The schematic drawing for the fine structure of exciton states in LHPs. (c) and (d) The band edge photoexcitation *via* the circularly polarized light, and the spin-photogalvanic measurement. Experimental results of photo-induced EPR spectra for $(R\text{-MBA})_2PbI_4$ single crystals measured at (e) 300 K and (f) 150 K. The photoexcitation wavelength and the laser power were 405 nm and 90 mW, respectively. (g) The experimental result of the GIWAX spectrum for the $(S\text{-MBA})_2PbI_4$ polycrystalline thin film. The similar spectrum could be obtained for the $(R\text{-MBA})_2PbI_4$ polycrystalline thin film.

In our case, the $\Gamma_5^{\pm}$ symmetry associated optical transitions can be effectively triggered for the $(R\text{-MBA})_2PbI_4$ and $(S\text{-MBA})_2PbI_4$ thin films.[46,57] Despite the spin-dependent optical transitions and crystalline orientation, another critical contribution is CISS for the electronic transport upon the dissociation of photogenerated exciton. Because of the inherent chiral-induced SOC, the conductive charges are spin-dependent. Only one spin channel that is either up or down dominates the conductive transport. This is also known as the Edelstein effect, which is concerned with a macroscopic spin polarization/magnetization due to the presence of chiral-induced SOC.[58] It connects the carrier spin with its spatial motion for the chiral LHPs in a macroscopic electrical field. Thus, we believe that the co-existence of both Rashba band and CISS are mutually responsible for the generation of considerable spin-photogalvanic effect for the chiral LHPs.

4. Conclusions

In this work, we have studied the spin-photogalvanic effect for typical chiral LHPs, such as $(R\text{-MBA})_2PbI_4$ and $(S\text{-MBA})_2PbI_4$. The pronounced CPGE and LPGE were measured in a wide temperate range from 4 K to 300 K. The constant in-plane magnetic fields can effectively manipulate the magnitude and sign for the effect. The spin-photogalvanic effect originates from the Rashba bands in the momentum vector space for the

material with SIA. The CISS property of the chiral LHPs can further contribute to the effect.

Data availability statement

The data that support the finding of the study are available from the corresponding author upon reasonable request.

Conflicts of interest

The authors declare no conflict of interest.

Acknowledgements

The work was supported by the Fundamental Research Funds for the Central Universities (2019RC101), the National Natural Science Foundation of China (Grant No. 61974010), and the Intergovernmental Cooperation Project, National Key Research and Development Program, Ministry of Science and Technology, China (Grant No. 2019YFE0108400).

References

1 Y. Bai, Z. Huang, X. Zhang, J. Lu, X. Niu, Z. He, C. Zhu, M. Xiao, Q. Song, X. Wei, *et al.*, Initializing film homogeneity to retard phase segregation for stable perovskite solar cells, *Science*, 2022, **378**, 747–754.

2 S. Sidhik, Y. Wang, M. De Siena, R. Asadpour, A. J. Torma, T. Terlier, K. Ho, W. Li, A. B. Puthirath, X. Shuai, *et al.*, Deterministic fabrication of 3D/2D perovskite bilayer stacks for durable and efficient solar cells, *Science*, 2022, **377**, 1425–1430.

3 Y. Zhao, F. Ma, Z. Qu, S. Yu, T. Shen, H.-X. Deng, X. Chu, X. Peng, Y. Yuan, X. Zhang, *et al.*, Inactive (PbI2)2RbCl stabilizes perovskite films for efficient solar cells, *Science*, 2022, **377**, 531–534.

4 K. Xiao, Y.-H. Lin, M. Zhang, R. D. J. Oliver, X. Wang, Z. Liu, X. Luo, J. Li, D. Lai, H. Luo, *et al.*, Scalable processing for realizing 21.7%-efficient all-perovskite tandem solar modules, *Science*, 2022, **376**, 762–767.

5 J. S. Kim, J.-M. Heo, G.-S. Park, S.-J. Woo, C. Cho, H. J. Yun, D.-H. Kim, J. Park, S.-C. Lee, S.-H. Park, *et al.*, Ultra-bright, efficient and stable perovskite light-emitting diodes, *Nature*, 2022, **611**, 688–694.

6 Z. Chu, Y. Zhao, F. Ma, C.-X. Zhang, H. Deng, F. Gao, Q. Ye, J. Meng, Z. Yin, X. Zhang, *et al.*, Large cation ethylammonium incorporated perovskite for efficient and spectra stable blue light-emitting diodes, *Nat. Commun.*, 2020, **11**, 4165.

7 X. Sun, C. Han, K. Wang, H. Yu, J. Li, K. Lu, J. Qin, H. Yang, L. Deng, F. Zhao, *et al.*, Effect of Bathocuproine Organic Additive on Optoelectronic Properties of Highly Efficient Methylammonium Lead Bromide Perovskite Light-Emitting Diodes, *ACS Appl. Energy Mater.*, 2018, **1**, 6992–6998.

8 X. Li, Y. Wu, S. Zhang, B. Cai, Y. Gu, J. Song and H. Zeng, CsPbX3 Quantum Dots for Lighting and Displays: Room-Temperature Synthesis, Photoluminescence Superiorities, Underlying Origins and White Light-Emitting Diodes, *Adv. Funct. Mater.*, 2016, **26**, 2435–2445.

9 J. Song, J. Li, X. Li, L. Xu, Y. Dong and H. Zeng, Quantum Dot Light-Emitting Diodes Based on Inorganic Perovskite Cesium Lead Halides (CsPbX3), *Adv. Mater.*, 2015, **27**, 7162–7167.

10 H. Xu, M. Wang, Z.-G. Yu, K. Wang and B. Hu, Magnetic field effects on excited states, charge transport, and electrical polarization in organic semiconductors in spin and orbital regimes, *Adv. Phys.*, 2019, **68**, 49–121.

11 Z. G. Yu, Effective-mass model and magneto-optical properties in hybrid perovskites, *Sci. Rep.*, 2016, **6**, 28576.

12 D. Niesner, M. Hauck, S. Shrestha, I. Levchuk, G. J. Matt, A. Osvet, M. Batentschuk, C. Brabec, H. B. Weber and T. Fauster, Structural fluctuations cause spin-split states in tetragonal (CH_3NH3)PbI3 as evidenced by the circular photogalvanic effect, *Proc. Natl. Acad. Sci. U. S. A.*, 2018, **115**, 9509–9514.

13 R.-H. Pan, X.-T. Tang, J.-P. Li, H.-M. Yu, B. Hu and K. Wang, Spin Transport and Magnetic Field Effects in Organic-inorganic Hybrid Perovskites, *Chin. J. Lumin.*, 2020, **41**, 753–769.

14 S. D. Stranks and P. Plochocka, The influence of the Rashba effect, *Nat. Mater.*, 2018, **17**, 381–382.

15 J. Even, L. Pedesseau, J.-M. Jancu and C. Katan, Importance of Spin–Orbit Coupling in Hybrid Organic/Inorganic Perovskites for Photovoltaic Applications, *J. Phys. Chem. Lett.*, 2013, **4**, 2999–3005.

16 A. Filippetti, P. Wadhwa, C. Caddeo and A. Mattoni, A promising outlook on the development of lead halide perovskites as spin-orbitronic materials, *Appl. Phys. Lett.*, 2022, **121**, 200501.

17 K. Wang, Q. Yang, J. Duan, C. Zhang, F. Zhao, H. Yu and B. Hu, Spin-Polarized Electronic Transport through Ferromagnet/Organic–Inorganic Hybrid Perovskite Spinterfaces at Room Temperature, *Adv. Mater. Interfaces*, 2019, **6**, 1900718.

18 C. Zhang, D. Sun, C. X. Sheng, Y. X. Zhai, K. Mielczarek, A. Zakhidov and Z. V. Vardeny, Magnetic field effects in hybrid perovskite devices, *Nat. Phys.*, 2015, **11**, 428–435.

19 Y.-C. Hsiao, T. Wu, M. Li and B. Hu, Magneto-Optical Studies on Spin-Dependent Charge Recombination and Dissociation in Perovskite Solar Cells, *Adv. Mater.*, 2015, **27**, 2899–2906.

20 J. Y. Wang, C. Zhang, H. L. Liu, R. McLaughlin, Y. X. Zhai, S. R. Vardeny, X. J. Liu, S. McGill, D. Semenov, H. W. Guo, *et al.*, Spin-optoelectronic devices based on hybrid organic-inorganic trihalide perovskites, *Nat. Commun.*, 2019, **10**(1), 129.

21 G. K. Long, R. Sabatini, M. I. Saidaminov, G. Lakhwani, A. Rasmita, X. G. Liu, E. H. Sargent and W. B. Gao, Chiral-

perovskite optoelectronics, *Nat. Rev. Mater.*, 2020, **5**, 423–439.

22 G. Long, C. Jiang, R. Sabatini, Z. Yang, M. Wei, L. N. Quan, Q. Liang, A. Rasmita, M. Askerka, G. Walters, *et al.*, Spin control in reduced-dimensional chiral perovskites, *Nat. Photonics*, 2018, **12**, 528–533.

23 J. Ahn, E. Lee, J. Tan, W. Yang, B. Kim and J. Moon, A new class of chiral semiconductors: chiral-organic-molecule-incorporating organic–inorganic hybrid perovskites, *Mater. Horiz.*, 2017, **4**, 851–856.

24 Y. Hu, F. Florio, Z. Chen, W. A. Phelan, M. A. Siegler, Z. Zhou, Y. Guo, R. Hawks, J. Jiang, J. Feng, *et al.*, A chiral switchable photovoltaic ferroelectric 1D perovskite, *Sci. Adv.*, 2020, **6**, eaay4213.

25 L. Zhang, J. Jiang, C. Multunas, C. Ming, Z. Chen, Y. Hu, Z. Lu, S. Pendse, R. Jia, M. Chandra, *et al.*, Room-temperature electrically switchable spin–valley coupling in a van der Waals ferroelectric halide perovskite with persistent spin helix, *Nat. Photonics*, 2022, **16**, 529–537.

26 D. Di Nuzzo, L. Cui, J. L. Greenfield, B. Zhao, R. H. Friend and S. C. J. Meskers, Circularly Polarized Photoluminescence from Chiral Perovskite Thin Films at Room Temperature, *ACS Nano*, 2020, **14**, 7610–7616.

27 C. Yuan, X. Li, S. Semin, Y. Feng, T. Rasing and J. Xu, Chiral Lead Halide Perovskite Nanowires for Second-Order Nonlinear Optics, *Nano Lett.*, 2018, **18**, 5411–5417.

28 R. Pan, K. Wang and Z.-G. Yu, Magnetic-field manipulation of circularly polarized photoluminescence in chiral perovskites, *Mater. Horiz.*, 2022, **9**, 740–747.

29 H. Lu, J. Wang, C. Xiao, X. Pan, X. Chen, R. Brunecky, J. J. Berry, K. Zhu, M. C. Beard and Z. V. Vardeny, Spin-dependent charge transport through 2D chiral hybrid lead-iodide perovskites, *Sci. Adv.*, 2019, **5**, eaay0571.

30 W. Su and F. Yuan, Opportunities and challenges of chiral perovskites for spin-LEDs, *Trends Chem.*, 2022, **4**, 965–968.

31 W. Su and F. Yuan, Chiral perovskites for room-temperature spin light-emitting diodes, *Sci. Bull.*, 2022, **67**, 1535–1538.

32 H. Lu, Z. V. Vardeny and M. C. Beard, Control of light, spin and charge with chiral metal halide semiconductors, *Nat. Rev. Chem.*, 2022, **6**, 470–485.

33 C. Zhang, D. Sun, Z.-G. Yu, C.-X. Sheng, S. McGill, D. Semenov and Z. V. Vardeny, Field-induced spin splitting and anomalous photoluminescence circular polarization in $CH_3NH3PbI3$ films at high magnetic field, *Phys. Rev. B: Condens. Matter Mater. Phys.*, 2018, **97**, 134412.

34 Z. G. Yu, Chirality-Induced Spin-Orbit Coupling, Spin Transport, and Natural Optical Activity in Hybrid Organic-Inorganic Perovskites, *J. Phys. Chem. Lett.*, 2020, **11**, 8638–8646.

35 R. Pan, S. Tao, L. Kan, J. Hu, J. Li, Y. Li, X. Zhang and K. Wang, Tunable and Large Magneto-Photoluminescence for Single-Crystalline Chiral Perovskites, *Adv. Opt. Mater.*, 2022, **10**, 2200064.

36 S. D. Ganichev, E. L. Ivchenko, V. V. Bel'kov, S. A. Tarasenko, M. Sollinger, D. Weiss, W. Wegscheider and W. Prettl, Spin-galvanic effect, *Nature*, 2002, **417**, 153–156.

37 S. D. Ganichev and W. Prettl, Spin photocurrents in quantum wells, *J. Phys.: Condens. Matter*, 2003, **15**, R935.

38 T. Feng, Z. Wang, Z. Zhang, J. Xue and H. Lu, Spin selectivity in chiral metal–halide semiconductors, *Nanoscale*, 2021, **13**, 18925–18940.

39 X. Liu, A. Chanana, U. Huynh, F. Xue, P. Haney, S. Blair, X. Jiang and Z. V. Vardeny, Circular photogalvanic spectroscopy of Rashba splitting in 2D hybrid organic–inorganic perovskite multiple quantum wells, *Nat. Commun.*, 2020, **11**, 323.

40 J. W. Li and P. M. Haney, Circular photogalvanic effect in organometal halide perovskite $CH_3NH3PbI3$, *Appl. Phys. Lett.*, 2016, **109**, 573–578.

41 J. S. Lee, G. A. H. Schober, M. S. Bahramy, H. Murakawa, Y. Onose, R. Arita, N. Nagaosa and Y. Tokura, Optical Response of Relativistic Electrons in the Polar BiTeI Semiconductor, *Phys. Rev. Lett.*, 2011, **107**, 117401.

42 H. Yuan, X. Wang, B. Lian, H. Zhang, X. Fang, B. Shen, G. Xu, Y. Xu, S.-C. Zhang, H. Y. Hwang, *et al.*, Generation and electric control of spin–valley-coupled circular photogalvanic current in WSe2, *Nat. Nanotechnol.*, 2014, **9**, 851–857.

43 J. W. McIver, D. Hsieh, H. Steinberg, P. Jarillo-Herrero and N. Gedik, Control over topological insulator photocurrents with light polarization, *Nat. Nanotechnol.*, 2012, **7**, 96–100.

44 V. Lechner, L. E. Golub, F. Lomakina, V. V. Bel'kov, P. Olbrich, S. Stachel, I. Caspers, M. Griesbeck, M. Kugler, M. J. Hirmer, *et al.*, Spin and orbital mechanisms of the magnetogyrotropic photogalvanic effects in GaAs/AlxGa1-xAs quantum well structures, *Phys. Rev. B: Condens. Matter Mater. Phys.*, 2011, **83**, 155313.

45 P.-J. Huang, K. Taniguchi, M. Shigefuji, T. Kobayashi, M. Matsubara, T. Sasagawa, H. Sato and H. Miyasaka, Chirality-Dependent Circular Photogalvanic Effect in Enantiomorphic 2D Organic–Inorganic Hybrid Perovskites, *Adv. Mater.*, 2021, **33**, 2008611.

46 R. Pan, J. Hu, S. Tao, L. Kan, H. Yu and K. Wang, Impact of crystal growth diversity on magneto-photoluminescence and circular dichroism in chiral lead halide perovskites, *J. Mater. Chem. C*, 2022, **10**, 16706–16713.

47 H. P. Lu, J. Y. Wang, C. X. Xiao, X. Pan, X. H. Chen, R. Brunecky, J. J. Berry, K. Zhu, M. C. Beard and Z. V. Vardeny, Spin-dependent charge transport through 2D chiral hybrid lead-iodide perovskites, *Sci. Adv.*, 2019, **5**, eaay0571.

48 P. A. Obraztsov, D. Lyashenko, P. A. Chizhov, K. Konishi, N. Nemoto, M. Kuwata-Gonokami, E. Welch, A. N. Obraztsov and A. Zakhidov, Ultrafast zero-bias photocurrent and terahertz emission in hybrid perovskites, *Commun. Phys.*, 2018, **1**, 14.

49 G. B. Osterhoudt, L. K. Diebel, M. J. Gray, X. Yang, J. Stanco, X. Huang, B. Shen, N. Ni, P. J. W. Moll, Y. Ran, *et al.*, Colossal mid-infrared bulk photovoltaic effect in a type-I Weyl semimetal, *Nat. Mater.*, 2019, **18**, 471–475.

50 Z. J. Huang, B. P. Bloom, X. J. Ni, Z. N. Georgieva, M. Marciesky, E. Vetter, F. Liu, D. H. Waldeck and D. L. Sun, Magneto-Optical Detection of Photoinduced Magnetism via Chirality-Induced Spin Selectivity in 2D Chiral Hybrid Organic-Inorganic Perovskites, *ACS Nano*, 2020, **14**, 10370–10375.

51 D. Niesner, M. Wilhelm, I. Levchuk, A. Osvet, S. Shrestha, M. Batentschuk, C. Brabec and T. Fauster, Giant Rashba Splitting in $CH_3NH3PbBr3$ Organic-Inorganic Perovskite, *Phys. Rev. Lett.*, 2016, **117**, 126401.

52 Y. Zhai, S. Baniya, C. Zhang, J. Li, P. Haney, C.-X. Sheng, E. Ehrenfreund and Z. V. Vardeny, Giant Rashba splitting in 2D organic-inorganic halide perovskites measured by transient spectroscopies, *Sci. Adv.*, 2017, **3**, e1700704.

53 S. B. Todd, D. B. Riley, A. Binai-Motlagh, C. Clegg, A. Ramachandran, S. A. March, J. M. Hoffman, I. G. Hill, C. C. Stoumpos, M. G. Kanatzidis, *et al.*, Detection of Rashba spin splitting in 2D organic-inorganic perovskite via precessional carrier spin relaxation, *APL Mater.*, 2019, **7**, 081116.

54 Z.-G. Yu, The Rashba effect and indirect electron–hole recombination in hybrid organic–inorganic perovskites, *Phys. Chem. Chem. Phys.*, 2017, **19**, 14907–14912.

55 M. Kim, J. Im, A. J. Freeman, J. Ihm and H. Jin, Switchable S=1/2 and J=1/2 Rashba bands in ferroelectric halide perovskites, *Proc. Natl. Acad. Sci. U. S. A.*, 2014, **111**, 6900–6904.

56 V. P. Solntsev, R. I. Mashkovtsev, A. V. Davydov and E. G. Tsvetkov, EPR study of coordination of Ag and Pb cations in BaB2O4 crystals and barium borate glasses, *Phys. Chem. Miner.*, 2008, **35**, 311–320.

57 K. Tanaka, T. Takahashi, T. Kondo, K. Umeda, K. Ema, T. Umebayashi, K. Asai, K. Uchida and N. Miura, Electronic and Excitonic Structures of Inorganic–Organic Perovskite-Type Quantum-Well Crystal (C4H9NH3)2PbBr4, *Jpn. J. Appl. Phys.*, 2005, **44**, 5923–5932.

58 V. M. Edelstein, Spin polarization of conduction electrons induced by electric current in two-dimensional asymmetric electron systems, *Solid State Commun.*, 1990, **73**, 233–235.

